Atomic Diffusion Induced by Electron-Beam Irradiation: An *in Situ* Study of Ag Structures Grown from α-Ag₂WO₄

Júlio C. Sczancoski,*,[†] Santiago Maya-Johson,[‡] Wyllamanney da Silva Pereira,[†] Elson Longo,[†] and Edson R. Leite[†,§]

[†]Universidade Federal de São Carlos (UFSCar), Department of Chemistry, São Carlos-SP, Brazil
[‡]Universidade Federal de São Carlos (UFSCar), Department of Materials Engineering, São Carlos-SP, Brazil
[§]Brazilian Nanotechnology National Laboratory (LNNano), CNPEM, Campinas-SP, Brazil

Ⓢ *Supporting Information*
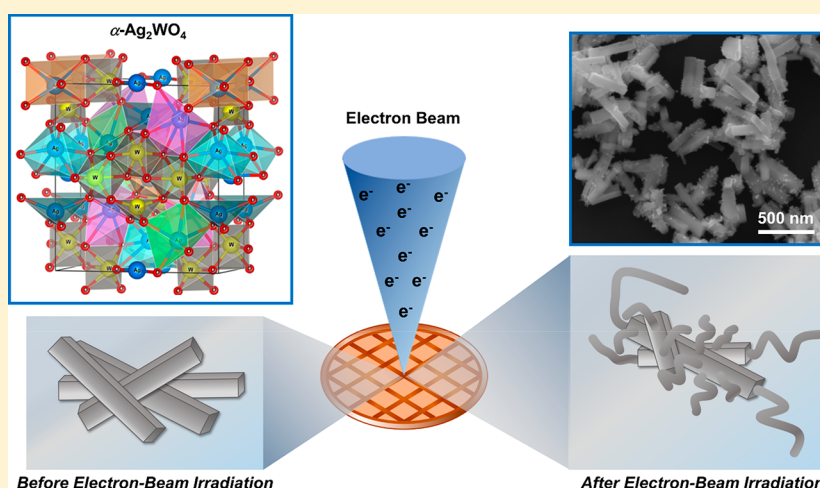
ABSTRACT: In this paper, we investigate the structural and morphological changes caused by the electron-beam irradiation that led to the growth of complex extruded filaments on the surfaces of α-Ag₂WO₄. To provide a complete description of this phenomenon, both scanning electron microscope (SEM) and transmission electron microscope (TEM) were employed in this study. Our experimental results evidenced that the extruded material was able to exhibit growth on different crystallographic faces, depending on the kind of microscope adopted during the electron-beam irradiation. For a more complete analysis, different electron-beam current densities in TEM were used to investigate all *in situ* modifications in the microcrystals. For the first time, besides the metallic silver, the presence of silver oxides (Ag₂O and Ag₃O₄) were detected in the composition of extruded material. The diffusion mechanisms related to morphological modifications in the samples irradiated in SEM and TEM were discussed in detail. The coprecipitation reaction in dimethyl sulfoxide was chosen as the synthetic route, which favored the appearance of rectangular rod-like α-Ag₂WO₄ microcrystals. A growth mechanism was proposed to explain the formation and growth processes of these microcrystals.

1. INTRODUCTION

In recent years, silver-based pure and hybrid materials have attracted considerable attention of several research groups and diverse industrial fields because of the wide variety of technological applications, which include mainly the following: photocatalysts for the degradation of organic pollutants in wastewater,[1−7] molecular labels in chromogenic reaction for tumor marker detection,[8] antibacterial/antifungal agents to combat bacteria/fungi responsible for some infectious diseases harmful to human health,[9−12] photoelectrochemical semiconductors to produce hydrogen via water splitting,[13−16] substrates in surface-enhanced Raman scattering analysis for the detection of molecules in complex matrices,[17] and so on.

Currently, one of the most promising silver-based materials for these multifunctional purposes is the silver tungstate (Ag₂WO₄).[18−20] According to a study carried out by van den Berg et al.,[21] this tungstate has three polymorphic forms: (a) orthorhombic phase (α) with space group *Pn2n* (thermodynamically stable), (b) hexagonal phase (β) with space group *P6₃/m* (metastable), and (c) cubic spinel-type phase (γ) with space group *Fd3m* (metastable). Besides polymorphism, another amazing behavior verified in these tungstates is the complex growth of silver (Ag) filaments emerging from the

surface of Ag_2WO_4 crystals, when exposed to electron-beam irradiation.[22−26]

The physicochemical properties of any material are controlled by a set of parameters, such as particle size, shape, agglomeration state, chemical composition, crystal structure, surface area, and chemistry.[27−30] Analyzing from the point of view of bulk and surface features, the physicochemical properties of Ag_2WO_4 can be tailored by understanding all stages involved in the growth process of Ag nanostructures. A considerable number of published papers, based on experimental evidence and/or theoretical data, has tried to elucidate the key factors responsible for the origin of this phenomenon. For example, Longo et al.[11] described that the excess of electrons, during the direct electron-beam irradiation, is able to provoke electronic and structural changes in α-Ag_2WO_4 crystals. This structural instability was considered the main responsible for the growth of metallic Ag filaments and appearance of oxygen (O) and Ag vacancies. The absence of α-Ag_2WO_4/Ag interfaces was interpreted as the formation of a continuous hybrid structure (semiconductor-metal junction).

In another interesting study, San-Miguel et al.[31] explained that there is a predominant growth of Ag on the (001) surface of α-Ag_2WO_4 crystals. According to these authors, Ag species (with different coordination numbers) found in this specific surface have a predisposition to growth as metallic Ag nanostructures in pathways with a low energy barrier (less than 0.1 eV). As these Ag species migrate toward the surface, Ag vacancies are created in the bulk. In the interpretation of Longo et al.,[22] the driving force responsible for the redox process is arising from order−disorder effects on the clusters belonging to the Ag_2WO_4 structure. Based on the scientific evidence, the understanding of *in situ* electron-beam-induced modifications in Ag_2WO_4 crystals represents a paradigm in materials science, mainly in terms of electron-beam manipulation protocols (total current, acceleration voltage, current density, and so on). A precise analysis of this curious phenomenon in Ag_2WO_4 has great importance to describe the origin of Ag nanostructures grown on the surface of other Ag-based materials.[32−34]

In terms of morphological aspects, Ag_2WO_4 has a strong natural tendency in forming one-dimensional microparticles, for example, wires and rods.[35,36] The most traditional experimental methods employed for the preparation of these microparticles are microwave-assisted hydrothermal,[37,38] conventional hydrothermal,[39,40] sonochemical route,[41−43] and coprecipitation reaction (CR).[44−46] Among these chemical synthetic techniques, CR is more interesting because of its simplicity, cost-effectiveness, and unnecessary use of harmful organic solvents/reagents.[30] The CR proceeds via a burst of nucleation followed by growth stages, coarsening, and/or agglomeration processes of nanoparticles.[47] In recent years, polymeric or surfactant molecules have been dispersed in solvent media to prepare the Ag_2WO_4 via CR, mainly with the fundamental aim of controlling the particle sizes and finding new particle shapes in order to improve the physicochemical properties of this material.[48,49] Another viable strategy to change the morphological features of this tungstate is to employ other kinds of chemical solvents, for example, the dimethyl sulfoxide (DMSO). The DMSO is suitable for the synthesis of inorganic materials because of its unique features, such as polar aprotic solvent, stabilizing dispersion medium, excellent solvating power, high dielectric constant (46.5), nontoxicity, miscibility with water in all proportions, slightly

high boiling point (189 °C), and large latent heat of evaporation (53 kJ/mol at 25 °C).[50−54] All these features have played an essential role for the controlled growth of several nanostructured oxides.[55−60]

Therefore, in the present study, α-Ag_2WO_4 powders were synthesized via CR by using a fast injection-based method. The investigation was mainly focused on the structural and morphological changes in α-Ag_2WO_4 microcrystals by the electron-beam irradiation in scanning electron microscope (SEM) and transmission electron microscope (TEM). Based on the experimental results, the difference in energy of the electron beam in both types of microscopes resulted in distinct nucleation and growth processes of extruded Ag filaments. For a more detailed study, the electron-beam current density (EBCD) in TEM was varied from 2.5 A/m^2 to 42 A/m^2, so that all growth stages of the extruded material were carefully monitored in real time and recorded in videos.

2. MATERIALS AND METHODS

2.1. Synthesis. α-Ag_2WO_4 microcrystals were synthesized via CR by using a fast injection-based method. Sodium tungstate dihydrate [$Na_2WO_4 \cdot 2H_2O$] (99%, Aldrich) and silver nitrate [$AgNO_3$] (99.8%, Cennabras) were chosen as chemical starting precursors and used without further purification. For a typical synthesis, 2 mmol of $AgNO_3$ were dissolved in 80 mL of DMSO (Synth) contained in an angled three-neck round-bottom flask connected to a condenser and a thermocouple. This solution was maintained under constant stirring at 120 °C for 5 min. In a beaker, 1 mmol of $Na_2WO_4 \cdot 2H_2O$ was solubilized in 20 mL of deionized water, which was stirred at room temperature for 10 min. This procedure was adopted because the $Na_2WO_4 \cdot 2H_2O$ is insoluble in DMSO. This liquid medium (containing Na^+ and $WO_4^{2−}$ ions) was sucked with a plastic syringe (maximum capacity of 60 mL) and then quickly injected into the DMSO (containing Ag^+ ions). The water instantaneously evaporated during contact with the heated DMSO, so that the interaction between Ag^+ and $WO_4^{2−}$ ions resulted in a burst of nucleation. After this stage, the system was stirred for another 10 min at 120 °C. After naturally cooling to room temperature, the solid precipitates were separated from the liquid phase via centrifugation (7000 rpm for 5 min), washed with deionized water and acetone (ten times), and dried in a lab oven at 50 °C for 12 h.

2.2. Characterizations. The structural analysis of α-Ag_2WO_4 microcrystals was performed via X-ray diffraction (XRD) by using a D/Max-2500PC diffractometer (Rigaku, Japan) with Cu Kα radiation ($\lambda = 0.154184$ nm). Data were collected over 2θ ranging from 10° to 110° with a scanning scan rate and step size of 0.2°/min and 0.02°, respectively. X-ray photoelectron spectroscopy (XPS) was performed by using an ESCA + spectrometer (ScientaOmicron, Germany) with a high-performance hemispheric analyzer (EA 125) adjusted to a pass energy of 50 eV. A monochromatic Al Kα radiation (1486.6 eV) was used as an excitation source. The operating pressure in the ultrahigh vacuum chamber during the XPS analysis was maintained at around 2 × 10^{-9} mbar. Energy steps of 0.5 and 0.05 eV were used for survey and high-resolution spectra, respectively. The binding energies in all spectra were calibrated in reference to the C 1s peak (284.8 eV). The W 4f, Ag 3d, and O 1s core levels were measured in high-resolution mode. CasaXPS software[61] was used to analyze the XPS spectra, in which the core-level signals were individually fitted with Gaussian−Lorentzian functions and background subtraction according to the Shirley method. The morphological aspects were examined by using an Inspect F50 scanning electron microscope equipped with a Schottky Field Emission source (FE-SEM) and a TECNAI G2 F20 transmission electron microscope (TEM) (both from Philips-FEI, Netherlands). For *in situ* analysis in FE-SEM of extruded Ag structures grown from α-Ag_2WO_4 microcrystals, the microscope was operated with an accelerating voltage of 10 kV, spot size of 3, work distance of approximately 10 mm, and by using secondary electron detectors (ETD, Everhart−Thornley Detector).

In the case of TEM, an FEI Tecnai G2 F20 X-TWIN (200 kV) with a Gatan CCD camera was used for the video acquisition. The samples were initially prepared by using 30 mg of α-Ag_2WO_4 dispersed in 4 mL of acetone via ultrasonication. The copper TEM grids with carbon film (3 nm) were rapidly submerged in this dispersion and then dried in vacuum for 12 h (vacuum chamber protected from ultraviolet irradiation). Before the insertion of the sample inside the microscope, the spot size was changed to 4, and the EBCD was reduced (at around 6 A/m^2). All alignments and EBCD optimizations were performed on a square of the TEM grid, different from that used to record the videos. In our test conditions, the diameter of the electron-beam did not exceed a square of the mesh. The videos were recorded in a new region, located two squares away from the alignment zone. The delay of a few seconds between arrival on a new zone and the start of the video recording (due to the search by representative particles and focus adjustment) did not have a significant influence on the growth of extruded Ag structures in the microcrystals because of the low EBCD ($\approx$ 6 A/m^2). Several minutes of exposure of the sample at low EBCD were necessary for the growth of Ag structures to be representative. The original videos were recorded at a frame rate of 8 fps with a resolution of 480 × 480.

For the experimental tests involving both FE-SEM and TEM, the previously prepared copper TEM grid was fixed in an aluminum stub with carbon conductive tape. This stub was placed inside the FE-SEM, which was operated by using an accelerating voltage of 10 kV, a spot size of 3.5, a work distance of 10 mm, and a dwell time of 300 μs. All microcrystals found in the four central squares of the grid were individually irradiated with the electron beam for 10 min. Posteriorly, this grid was placed inside the TEM and irradiated with an EBCD of 6000 A/m^2 for 20 min.

3. RESULTS AND DISCUSSION

3.1. Structural Ordering.
The Rietveld refinement plot of α-Ag_2WO_4 is displayed in Figure S1a (Support Information (SI)). According to our results, α-Ag_2WO_4 was well-characterized by an orthorhombic structure with space group $Pn2n$, exhibiting the lattice parameters $a = 10.89$ Å, $b = 12.01$ Å, and $c = 05.89$ Å as well as a unit cell volume of 770.34 Å^3. These structural data are in perfect agreement with other published studies.[10,25,62,63]

Another way of analyzing the final refinement results is to model the crystalline structure of this tungstate in a visualization program for structural models. Thus, our Rietveld refinement data were used as input parameters in VESTA software.[64] The three-dimensional simulation of α-Ag_2WO_4 revealed seven distinct clusters (one for W—O bonds and six for Ag—O bonds). From a general point of view, all W atoms are bonded to six O atoms, resulting in distorted octahedral [WO_6] clusters. On the other hand, Ag atoms are coordinated to two, four, six and seven O atoms, forming [AgO_2], [AgO_4], [AgO_6], and [AgO_7] clusters, respectively.[25] There are three kinds of [AgO_6] clusters, which differ in bond lengths and angles associated with O—Ag—O bonds (Figure S1b in SI).

Another important aspect to be considered is that diffraction peaks related to secondary phases were not detected in XRD patterns, which could diverge the final refinement results. There is difficulty inherent in determining by means of XRD diffractograms any secondary phase below 3% in a crystalline material. For example, some published papers[10−12] have demonstrated the formation and growth of irregular metallic Ag filaments on the surface of α-Ag_2WO_4. If this quantity is less than the limit imposed by the XRD technique, it is necessary to use other instrumental analyses to assist in the structural investigation. Thus, XPS can be considered one of the fundamental characterization techniques for this specific purpose.

3.2. X-ray Photoelectron Spectroscopy (XPS).
The surface oxidation states and chemical composition of as-prepared samples were analyzed by XPS. As shown in Figure S2a, the XPS survey spectrum revealed only the presence of peaks associated with Ag, W, and O. Cavinato et al.[65] and Xie et al.[66] reported several high-resolution XPS spectra for a variety of W species, which are very useful for a qualitative identification of W oxidation states in other materials (containing traces of this element in their composition). In our XPS spectrum for the W (Figure S2b), three peaks were identified by means of the fitting with Gaussian−Lorentzian functions (G-L components). The first most intense peak located at 34.70 eV is assigned to W $4f_{7/2}$, while the other doublet peaks with binding energies at 36.80 and 39.80 eV are due to W $4f_{5/2}$ and W $5p_{3/2}$, respectively.[66−70] All these W 4f core levels correspond to the W^{6+} oxidation state arising from W—O bonds in octahedral [WO_6] clusters.[24]

Two Ag 3d core level signals were detected in the XPS spectrum (Figure S2c), and they are directly related to Ag $3d_{5/2}$ and Ag $3d_{3/2}$. Each of these levels were perfectly fitted into two G-L components, which were found at 367.60 and 368.70 eV for Ag $3d_{5/2}$ and at 373.60 and 374.70 eV for Ag $3d_{3/2}$, respectively. The components at 367.60 and 373.60 eV arise from the Ag$^+$ oxidation state of Ag—O bonds in [AgO_n] clusters (n = 2, 4, 6, and 7). On the other hand, both low-intensity components detected at 368.70 and 374.70 eV are caused by the Ag^0 oxidation state.[20,24,41,49,71,72] In principle, as Rietveld refinement did not detect the presence of any secondary phase (Figure S1a), we suppose that the Ag^0 signals in the XPS spectrum are caused by metallic Ag sites randomly distributed on the surface of the samples. Therefore, the chosen preparation route by using DMSO as solvent was not able to completely avoid the reduction from Ag$^+$ to Ag^0.

In addition, three G-L components were needed to obtain a good fit for deconvolution of the O 1s envelope (Figure S2d). According to the literature,[24,73−75] the component at 529.80 eV is due to W—O bonds in [WO_4] clusters, while the other two verified at 531.45 and 533.25 eV are usually attributed to the hydroxyl group (−OH) and O species (O_2^-) chemisorbed on the surface of α-Ag_2WO_4, respectively

3.3. Morphological Aspects.
The low- and high-magnification FE-SEM micrographs revealed that the α-Ag_2WO_4 powders are composed of several rectangular rod-like microcrystals (Figure 1a−b). According to the theoretical calculation based on the Wulff construction,[76] α-Ag_2WO_4 microcrystals are typically characterized by (100) and (001) side facets and (010) end facets. When water is adopted as solvent in a CR maintained at around 90 °C, these microcrystals have showed (010) facets with hexagon-like shape.[22,23,62] In contrast, a remarkable feature observed in our α-Ag_2WO_4 microcrystals was the occurrence of (010) facets with rectangular-like shape (dotted green circles and inset in Figure 1b). Hence, both DMSO and synthesis temperature (120 °C) were responsible for this morphological change. A crystal growth mechanism was proposed in order to elucidate the formation and growth stages of these microcrystals. More details are presented in Figure S3 (SI).

The quantitative analysis of the particle size distribution (height and width) of these microcrystals revealed an average height ranging from 0.27 to 0.62 μm (26% at around 0.47 μm) and an average width ranging from 0.07 to 0.15 μm (20% at around 0.11 μm) (Figure 1c−d). The geometric dimensions of the microcrystals are smaller than those reported by
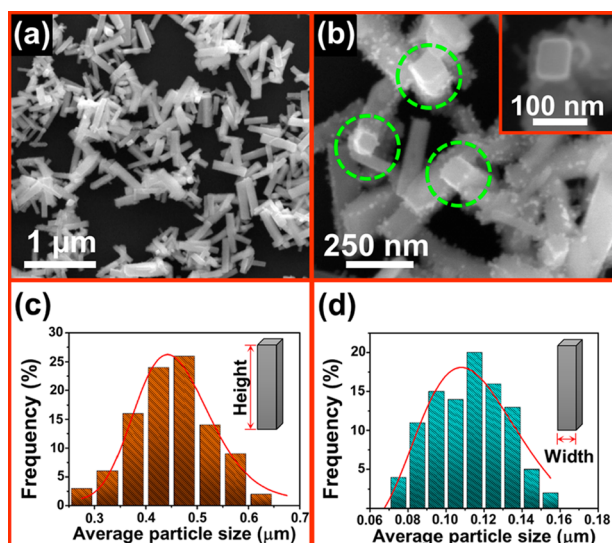
Figure 1. Low (a) and high-magnification (b) FE-SEM micrographs of rectangular rod-like α-Ag$_2$WO$_4$ microcrystals, respectively. The green dotted circles and inset in (b) show the (010) end facets with rectangular-like shape. Average particle size distribution (height and width) of α-Ag$_2$WO$_4$ microcrystals (c,d).

Cavalcante et al.[25] This behavior reflects the impact caused by the DMSO molecules in the morphological behavior of rectangular rod-like α-Ag$_2$WO$_4$ microcrystals.

A temporal analysis was performed by FE-SEM (accelerating voltage of 10 kV and spot size of 3) with the intention of detecting any occurrence of extruded filaments on the surface of α-Ag$_2$WO$_4$ microcrystals by the direct incidence of the electron beam. The initial time or 0 min was considered the exact instant in which the electron beam was focused on the selected region of the sample (Figure S4a). During the first 5 min of irradiation (Figure S4b), a fast and spontaneous matter transport (as irregular filaments) emerged from the surface of these microcrystals. Practically, no significant evolution was detected in the growth of these nanostructures for exposure periods from 10 to 25 min (Figure S4c−f). In a preliminary analysis, the structural and morphological modifications provoked by the electron beam in α-Ag$_2$WO$_4$ microcrystals are practically inevitable. An interesting observation is that the growth of extruded filaments preferentially progressed on (100) and (001) facets. These complex structures were not found on (010) facets of the microcrystals (Figure 1a−b and S4a−f). A similar phenomenon has been verified in hexagonal rod-like α-Ag$_2$WO$_4$ microcrystals synthesized in aqueous medium, when analyzed from the point of view of FE-SEM images.[22,24] The growth of long Ag filaments on (010) facets was clearly noted in real-time TEM images. Nevertheless, the main scientific aim in these papers was not focused on this experimental evidence. To validate our assumption, we conducted a controlled experiment in TEM, in which the EBCD was carefully varied to identify whether there is a threshold situation or some modification in the growth kinetics of extruded Ag structures in the microcrystals by the electron-beam irradiation.

Figure 2 shows TEM snapshot images extracted from real-time videos (included in the SI), which reveal several rectangular rod-like α-Ag$_2$WO$_4$ microcrystals when exposed to the electron-beam irradiation at different EBCDs for 5 min. In all these situations, the electron beam was responsible for an
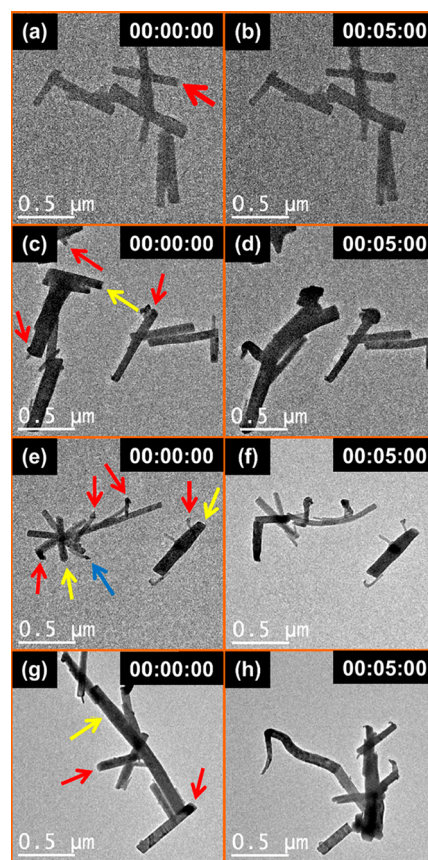
Figure 2. TEM snapshot images of α-Ag$_2$WO$_4$ microcrystals before and after being exposed to electron-beam irradiation for 5 min. The EBCD was maintained at 2.5 A/m^2 (a, b), 6 A/m^2 (c, d), 23 A/m^2 (e, f), and 42 A/m^2 (g, h), respectively. In these images were identified the following phenomena: growth of filaments or agglomerates on the surface of the microcrystals (red arrows), shrinkage of microcrystals (yellow arrows), and resorption of extruded material (blue arrows).

intense and dynamic matter diffusion along the microcrystals, resulting in preferential growth of long filaments or agglomerates on (010) facets (red arrows in Figure 2a,c,e,g). This transport phenomenon was most prominent and faster when high EBCDs were employed in these experiments. For example, when the sample was irradiated with low EBCD (approximately 2.5 A/m^2) (video SV1 in SI), longer times were necessary for the system to reach an equilibrium condition, i.e., when the matter mobility in the microcrystals was finally concluded (Figure 2a−b). This time was reduced when the electron dose was selectively increased (Figure 2c−h) (videos SV2, SV3, and SV4 in SI). Independent of the EBCD, we presume that the final result would be the same, i.e., a set of microcrystals containing an enormous amount of extruded material on their surfaces. This assumption was based on the study performed by Gong et al.,[77] in which Ag nanoparticles were synthesized by electron-beam irradiation. According to these authors, the growth of these nanoparticles was influenced by the EBCD, but was not affected by the exposition time. In addition, they reported that the critical EBCD found to grow the Ag nanoparticles was 1.5×10^4 A/m^2. This value is extremely superior to that adopted in our experiments (42 A/m^2). In our particular study, as previously mentioned, a high EBCD accelerated the matter transport, as can be seen in videos SV3 and SV4 in SI. Thus, α-Ag$_2$WO$_4$

microcrystals have reached the equilibrium state in approximately 20 min with an EBCD selected at 6 A/m^2, while, at 42 A/m^2, this time was less than 3 min. The choice of an EBCD that is a hundred times higher could promote a faster matter transport with the final growth of extruded structures in a few seconds. Hence, the evolution of time-dependent phenomena would be difficult to detect. It is important to emphasize that, according to previous studies,[22−24] the extruded material is abundantly composed of Ag atoms.

Additional impressive behavior was observed when the microcrystals were stacked, where contact areas acted as "bridges", forming a single system. These "bridges" provided a new and easy way for matter to flow from one microcrystal to another during the electron-beam irradiation. In some situations identified in this system, a substantial amount of atoms was able to migrate to only a microcrystal among the various available, as can be seen in Figure 2g−h and video SV4 in SI. From our understanding, the final amount of extruded material is independent of the EBCD, but intrinsically related to the total mass of all microcrystals (when they are connected) during the period of electron-beam irradiation.

Other two phenomena found with a lower occurrence were shrinkage of microcrystals (yellow arrows in Figures 2c,e,g) and reabsorption of nanostructures previously nucleated on the surface (blue arrow in Figure 2e). In the first case, the microcrystal (referred as to "mother") is shrunk once the electron beam initiates the atomic diffusion. As all microcrystals are composed of Ag, O, and W, low mobility of W atoms (lattice former) followed by the amorphization of the "mother" microcrystal is likely to happen. In relation to the second phenomenon, the nanostructures initially grow on the surface and they were posteriorly reabsorbed by the "mother" microcrystal due to the electronic conductivity imposed by the electron beam. This reabsorbed matter was able to migrate from the "mother" microcrystal to other neighbors, when contacts were created between them (blue arrow in both Figure 2e and video SV3 in SI).

Figure 3 shows TEM and high-resolution transmission electron microscopy (HRTEM) images as well as the elemental analyses obtained by using energy-dispersive X-ray spectroscopy (EDX) of microcrystals irradiated for 18 min with an EBCD of approximately 40 A/m^2. As expected, after interaction with the electron beam, a long and irregular filament grew as a function of the matter flow arising from several stacked microcrystals (Figure 3a). For a complete chemical analysis, two distinct regions were chosen in this system, the first one on the grown filament ((b) in yellow circle), and the second one on the "mother" microcrystal ((c) in yellow circle). EDX performed on the grown filament indicated an absolute predominance of Ag species in relation to O and W (Figure 3b). On the other hand, the "mother" microcrystal showed a high contribution of both W and O, and a small concentration of Ag (Figure 3c). These results suggest that the Ag atoms of the "mother" microcrystal migrated to form the extruded filaments (or agglomerates in some situations). Similar behavior was reported in a study published by Longo et al.[22]

HRTEM was fundamental in order to identify which Ag species or structures can be found along the filament. An HRTEM image was acquired on the tip of the filament (Figure 3d), so that the Fast Fourier Transform (FFT) in this region revealed the presence of spots (Figure 3e) corresponding to [111] and [200] planes of metallic Ag (cubic structure, JCPDS
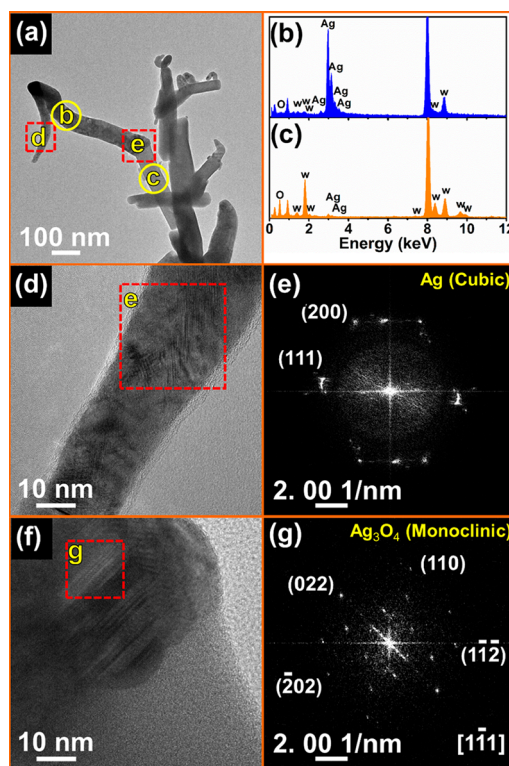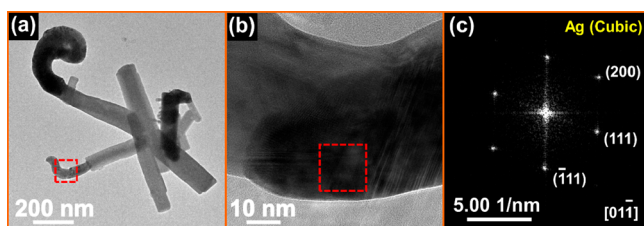

Figure 3. (a) TEM image of α-Ag$_2$WO$_4$ microcrystals irradiated at 40 A/m^2 for 18 min; (b−c) EDX spectra obtained on the grown filament (b in yellow circle in (a)) and "mother" microcrystal (c in yellow circle in (a)), respectively; (d) HRTEM image acquired on the tip of the grown filament (d in red dashed square in (a)); (e) FFT pattern corresponding to selected region in (d) (red dashed square); (f) HRTEM image acquired close to the interface filament/"mother" microcrystal (e in red dashed square in (a)); (g) FFT pattern corresponding to selected region in (f) (red dashed square).

card no. 01-001-1167).[78] No zone axis was identified, indicating that the extruded material is composed of several Ag crystals with different crystallographic orientations. For the HRTEM image taken close to the interface filament/"mother" microcrystal (Figure 3f), the FFT pattern was perfectly indexed to silver oxide (Ag$_3$O$_4$) (monoclinic structure, JCPDS card no. 01-077-1846),[78] which was oriented on the $[1\bar{1}1]$ zone axis (Figure 3g). In order to form the Ag$_3$O$_4$, O atoms were able to migrate for this region in the filament. Therefore, this interesting behavior implies that there is a collective diffusion of not only Ag atoms to grow the extruded nanostructures but also O species.

In another test with TEM, the electron-beam irradiations were conducted in two stages, which included changes in both EBCD and exposition time on the same group of microparticles. Initially, the irradiation was conducted at 40 A/m^2 for 10 min (Figure 4a) to induce the mobility as well as initial growth of Ag filaments. One of the filaments was selected (dotted red square in Figure 4a), and an HRTEM image was taken (Figure 4b). The FFT pattern acquired from the grown material showed typical reflections of metallic Ag (cubic structure) oriented along the $[11\bar{1}]$ zone axis (Figure 4c).

In the second part of this experiment, the EBCD increased up to 40 000 A/m^2 and was maintained for 24 min on the previously analyzed microcrystals (Figure 5a). Significant changes were detected in this system only in the irradiated local area; i.e., the extruded Ag filament started to shrink and

Figure 4. (a) TEM image of α-Ag$_2$WO$_4$ microcrystals irradiated at 40 A/m^2 for 10 min; (b) HRTEM image acquired on the grown filament (red dashed square in (a)); (c) FFT pattern corresponding to selected region in (b) (red dashed square).
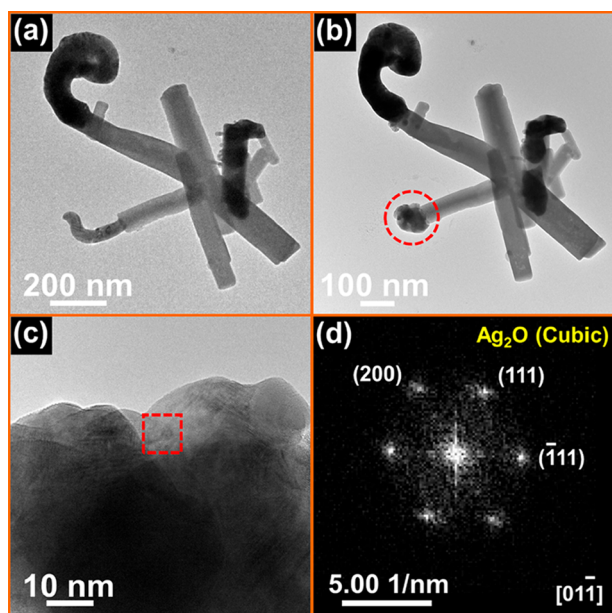
Figure 5. (a−b) TEM images of α-Ag$_2$WO$_4$ microcrystals irradiated at 6000 A/m^2 for 20 min and at 40 000 A/m^2 for 24 min, respectively; (c) HRTEM image of an aggregate (red dashed circle in (b)); (d) FFT pattern corresponding to selected region in (c) (red dashed square).

an aggregate was formed (Figure 5a−b and video SV5 in SI). From the beginning to end of this stage, a typical manifestation of the Ostwald ripening mechanism sometimes was evidenced,[79] in which the small crystals were dissolved (due to high dissolution and surface energy) and redeposited onto large crystals.[80,81] By indexing the FFT of the HRTEM image acquired on this aggregated system, the presence of crystallographic planes related to silver(I) oxide (Ag$_2$O) (cubic structure, JCPDS card no. 00-043-0997)[78] was confirmed (Figure 5c−d). It is further evidenced that there is also the atomic mobility of O species, together with the Ag atoms, during the growth of extruded structures on the surface of the microcrystals. In our knowledge, for the first time, the existence of Ag$_2$O or Ag$_3$O$_4$ in the arrangement of extruded filaments in α-Ag$_2$WO$_4$ microcrystals has been proven.

As previously demonstrated, FE-SEM and TEM techniques were able to induce the growth of extruded filaments in α-Ag$_2$WO$_4$ microcrystals by electron-beam irradiation. The fundamental difference is that these nanostructures preferentially grow on the (100) and (001) side facets in FE-SEM and on the (010) end facets in TEM. Based on this observation, a new test involving both FE-SEM and TEM was elaborated. The main intention was to investigate wherever local Ag

nucleation points (randomly distributed on (100) and (001) facets), initially grown by the electron-beam in FE-SEM, could act as preferential migration sites to grow the extruded structures when irradiated during TEM.

In order to perform this test, each of the microcrystals found on the four central squares of the TEM grid was first exposed to the electron beam in an FE-SEM (maintained at 10 kV) for 10 min. In the sequence, this grid was irradiated in a transmission electron microscope with an EBCD of 6000 A/m^2 for 20 min. As expected, FE-SEM yielded the growth of small points or filaments in the microcrystals; however, these microcrystals did not show any evolution process in terms of matter diffusion as well as on the growth of extruded filaments in TEM. Practically, the microcrystals remained in an equilibrium state (Figure S5). A brief comment that needs to be made is that high resolution FE-SEM images of α-Ag$_2$WO$_4$ microcrystals deposited on the copper TEM grid were not possible to acquire.

From analyzing all results obtained through the electron-beam irradiation, the key question that arises is *"Why the electron beam irradiation in FE-SEM and TEM causes distinct growth of extruded nanostructures in α-Ag$_2$WO$_4$ microcrystals?"* The answer can be associated with operating peculiarities of each of these microscopes. A common feature in both microscopes is that the electron beam transfers a fraction of their energy for the sample. Sometimes, this transferred energy is able to cause atomic mobility, surface defects, electrostatic charging, and local heating in the crystals.[82,83]

From the point of view of FE-SEM, the penetration depth of incident electrons in a sample is dependent on the energy of the electron beam and nature of the sample. Generally, for electrons accelerated with high energies up to 1 MeV, the penetration depth is approximately micrometers.[84,85] In our study, the electrons were accelerated at 10 kV (10 keV), ensuring a penetration depth of a few nanometers on the surface of α-Ag$_2$WO$_4$ microcrystals. When the fast electrons hit the microcrystals, local defects can be generated and an electronic conduction process on the surface can be initiated. These local defects (preferentially on (100) and (001) side facets) were able to accumulate a high amount of electrons (forming a negatively charged electrostatic field), inducing the mobility of Ag$^+$ ions (previously bonded to Ag−O−W clusters) via Coulombic attraction. These regions begin to act as nucleation sites driving the continuous growth of irregular Ag filaments.

In contrast, the electron beam in a transmission microscope was accelerated in 200 kV ($\approx$ 278 keV, considering relativistic calculations) by using an EBCD from 2.5 A/m^2 to 42 A/m^2. Consequently, the electrons were transmitted through the microcrystals. Therefore, there is an electronic conduction (charging effect) along the microcrystals with a high amount of electrons concentrated in their (010) end facets. Similarly as in FE-SEM, these regions rich in negative charges (negatively charged electrostatic field) attract the Ag$^+$ ions, causing the growth of irregular Ag filaments (or agglomerates). The reduction reaction promotes the appearance of long extruded filaments mainly composed of metallic Ag. However, in the areas of these filaments situated close to the interface of the "mother" microcrystal, there is also the presence of Ag$_2$O (cubic structure) or (Ag$_3$O$_4$) (monoclinic structure). We suppose two different hypotheses to explain the origin of these oxides in the composition of extruded material. The first one is the damage caused by the electron-beam irradiation promoted

the formation of defects (for example, vacancies) in the microcrystals. The O species were able to migrate through these defects until they bond with Ag species (Ag—O bonds), forming Ag_2O and Ag_3O_4. In the second one, after the appearance of extruded material, the continuous electron bombardment on these filaments again caused the formation of Ag^+ ($Ag^0 \rightarrow Ag^+$) by means of irradiation damage.[82] These Ag^+ ions were able to attract O^- ions (with low mobility), arising from amorphous "mother" microcrystals, forming Ag—O bonds. The atomic rearrangement of Ag—O bonds in $[AgO_n]$ clusters (n = 2, 4, 6, and 7) promoted the formation of Ag_2O and Ag_3O_4 in the extruded material. An explanation of the correlation between EBCD and damage accumulation is reported in the SI. Particularly, future studies based on cryogenic electron microscopy can be an alternative way to clarify and describe with more detail the changes caused by the electron beam in the local ordering and structural organization of α-Ag_2WO_4 microcrystals.

4. CONCLUSION

In summary, rectangular rod-like α-Ag_2WO_4 microcrystals were synthesized via coprecipitation reaction by using DMSO. The intense and well-defined diffraction peaks confirmed that the microcrystals have a high degree of crystallinity, i.e., a long-range structural ordering. According to Rietveld refinement data, α-Ag_2WO_4 microcrystals crystallized in an orthorhombic structure with space group $Pn2n$, without any trace of secondary phases. XPS spectra showed typical peaks associated with Ag, W, and O in the microcrystals, without other chemical species bonded to the surface. The Ag^0 signals in the Ag 3d spectrum were ascribed to local metallic Ag sites found on the surface of the microcrystals. These sites grew during the formation stages of α-Ag_2WO_4 microcrystals by the coprecipitation reaction. The growth of complex extruded nanostructures was noted in the microcrystals during exposure to electron-beam irradiation in FE-SEM and TEM. FE-SEM was responsible for the growth of extruded Ag filaments preferentially along (100) and (001) facets. The matter diffusion as well as final stabilization of these filaments was verified during the first 5 min of irradiation in FE-SEM (accelerating voltage of 10 kV and spot size of 3). On the other hand, TEM induced preferential growth of long filaments or agglomerates on (010) facets of the microcrystals. The EBCD influenced the growth rate of the extruded material. In samples irradiated with low EBCD, longer times were necessary for the system to reach a stable condition. The indexing of FFT patterns taken from HRTEM images revealed that the extruded materials are composed of cubic metallic Ag, cubic (Ag_2O), and monoclinic (Ag_3O_4) silver oxides. These results suggested that the electron beam induced an atomic diffusion of O and Ag species in the microcrystals. Real-time videos were recorded, in which different phenomena were observed during the electron-beam irradiation in TEM, such as growth of Ag filaments, shrinkage of microcrystals, and reabsorption of nanostructures previously nucleated on the surface. These videos also indicated that there is mass transport between stacked microcrystals, presenting typical behavior of the single particle system. The way in which these atoms migrate from one microcrystal to another is still unknown. Future TEM-based studies will be necessary in order to accurately describe the nature of this phenomenon.

ASSOCIATED CONTENT

Ⓢ Supporting Information

The Supporting Information is available free of charge on the ACS Publications website at DOI: 10.1021/acs.cgd.8b01076.

> Details related to Rietveld refinement, crystal growth mechanism, and electron dose rate and damage accumulation; additional figures (PDF)
>
> Video of sample irradiated with EBCD $\approx$ 2.5 A/m^2 (MPG)
>
> Video of sample irradiated with EBCD $\approx$ 6 A/m^2 (MPG)
>
> Video of sample irradiated with EBCD $\approx$ 23 A/m^2 (MPG)
>
> Video of sample irradiated with EBCD $\approx$ 42 A/m^2 (MPG)
>
> Video of sample irradiated with EBCD $\approx$ 40 000 A/m^2 (MPG)

AUTHOR INFORMATION

Corresponding Author

*E-mail: jcsfisica@gmail.com.

ORCID Ⓘ

Júlio C. Sczancoski: 0000-0002-8233-3268
Elson Longo: 0000-0001-8062-7791

Notes

The authors declare no competing financial interest.

ACKNOWLEDGMENTS

REFERENCES

(1) Wang, Z.; Zhang, J.; Lv, J.; Dai, K.; Liang, C. Plasmonic Ag_2MoO_4/AgBr/Ag composite: Excellent photocatalytic performance and possible photocatalytic mechanism. *Appl. Surf. Sci.* **2017**, *396*, 791−798.

(2) Zhang, J.; Lv, J.; Dai, K.; Liu, Q.; Liang, C.; Zhu, G. Facile and green synthesis of novel porous g-C_3N_4/Ag_3PO_4 composite with enhanced visible light photocatalysis. *Ceram. Int.* **2017**, *43* (1), 1522−1529.

(3) Xu, D.; Cheng, B.; Zhang, J.; Wang, W.; Yu, J.; Ho, W. Photocatalytic activity of Ag_2MO_4 (M = Cr, Mo, W) photocatalysts. *J. Mater. Chem. A* **2015**, *3* (40), 20153−20166.

(4) Dong, H.; Chen, G.; Sun, J.; Li, C.; Yu, Y.; Chen, D. A novel high-efficiency visible-light sensitive Ag_2CO_3 photocatalyst with universal photodegradation performances: Simple synthesis, reaction mechanism and first-principles study. *Appl. Catal., B* **2013**, *134−135*, 46−54.

(5) Wang, L.; Wang, L.; Chu, D.; Wang, Z.; Zhang, Y.; Sun, J. Tartaric acid-assisted synthesis of Ag_3PO_4 hollow microspheres with enhanced photocatalytic properties. *Catal. Commun.* **2017**, *88*, 53−55.

(6) Lv, J.; Dai, K.; Zhang, J.; Lu, L.; Liang, C.; Geng, L.; Wang, Z.; Yuan, G.; Zhu, G. In situ controllable synthesis of novel surface plasmon resonance-enhanced Ag_2WO_4/Ag/Bi_2MoO_6 composite for enhanced and stable visible light photocatalyst. *Appl. Surf. Sci.* **2017**, *391*, 507−515.

(7) Huo, Y.; Wang, Z.; Zhang, J.; Liang, C.; Dai, K. Ag SPR-promoted 2D porous g-C_3N_4/Ag_2MoO_4 composites for enhanced photocatalytic performance towards methylene blue degradation. *Appl. Surf. Sci.* **2018**, *459*, 271−280.

(8) Wang, X.; Zhang, B.; Li, J.; Chang, H.; Wei, W. A simple and fast chromogenic reaction based on Ag_3PO_4/Ag nanocomposite for tumor marker detection. *Talanta* **2017**, *175*, 229−234.

(9) de Oliveira, R. C.; de Foggi, C. C.; Teixeira, M. M.; da Silva, M. D.; Assis, M.; Francisco, E. M.; Pimentel, B. N.; Pereira, P. F.; Vergani, C. E.; Machado, A. L.; Andres, J.; Gracia, L.; Longo, E. Mechanism of Antibacterial Activity via Morphology Change of α-$AgVO_3$: Theoretical and Experimental Insights. *ACS Appl. Mater. Interfaces* **2017**, *9* (13), 11472−11481.

(10) Roca, R. A.; Sczancoski, J. C.; Nogueira, I. C.; Fabbro, M. T.; Alves, H. C.; Gracia, L.; Santos, L. P. S.; de Sousa, C. P.; Andres, J.; Luz, G. E.; Longo, E.; Cavalcante, L. S. Facet-dependent photo-catalytic and antibacterial properties of α-Ag_2WO_4 crystals: combining experimental data and theoretical insights. *Catal. Sci. Technol.* **2015**, *5* (8), 4091−4107.

(11) Longo, V. M.; De Foggi, C. C.; Ferrer, M. M.; Gouveia, A. F.; Andre, R. S.; Avansi, W.; Vergani, C. E.; Machado, A. L.; Andres, J.; Cavalcante, L. S.; Hernandes, A. C.; Longo, E. Potentiated electron transference in α-Ag_2WO_4 microcrystals with Ag nanofilaments as microbial agent. *J. Phys. Chem. A* **2014**, *118* (31), 5769−78.

(12) Foggi, C. C.; Fabbro, M. T.; Santos, L. P. S.; de Santana, Y. V. B.; Vergani, C. E.; Machado, A. L.; Cordoncillo, E.; Andrés, J.; Longo, E. Synthesis and evaluation of α-Ag_2WO_4 as novel antifungal agent. *Chem. Phys. Lett.* **2017**, *674*, 125−129.

(13) Cao, Q.; Yu, J.; Yuan, K.; Zhong, M.; Delaunay, J.-J. Facile and Large-Area Preparation of Porous Ag_3PO_4 Photoanodes for Enhanced Photoelectrochemical Water Oxidation. *ACS Appl. Mater. Interfaces* **2017**, *9* (23), 19507−19512.

(14) Currao, A.; Reddy, V. R.; van Veen, M. K.; Schropp, R. E.; Calzaferri, G. Water splitting with silver chloride photoanodes and amorphous silicon solar cells. *Photochem. Photobiol. Sci.* **2004**, *3* (11−12), 1017−25.

(15) Martin, D. J.; Liu, G.; Moniz, S. J.; Bi, Y.; Beale, A. M.; Ye, J.; Tang, J. Efficient visible driven photocatalyst, silver phosphate: performance, understanding and perspective. *Chem. Soc. Rev.* **2015**, *44* (21), 7808−28.

(16) Yi, Z.; Ye, J.; Kikugawa, N.; Kako, T.; Ouyang, S.; Stuart-Williams, H.; Yang, H.; Cao, J.; Luo, W.; Li, Z.; Liu, Y.; Withers, R. L. An orthophosphate semiconductor with photooxidation properties under visible-light irradiation. *Nat. Mater.* **2010**, *9* (7), 559−64.

(17) Fodjo, E. K.; Li, D.-W.; Marius, N. P.; Albert, T.; Long, Y.-T. Low temperature synthesis and SERS application of silver molybdenum oxides. *J. Mater. Chem. A* **2013**, *1* (7), 2558.

(18) Lemos, P. S.; Altomare, A.; Gouveia, A. F.; Nogueira, I. C.; Gracia, L.; Llusar, R.; Andres, J.; Longo, E.; Cavalcante, L. S. Synthesis and characterization of metastable β-Ag_2WO_4: an experimental and theoretical approach. *Dalton Trans* **2016**, *45* (3), 1185−91.

(19) Roca, R. A.; Lemos, P. S.; Gracia, L.; Andrés, J.; Longo, E. Uncovering the metastable γ-Ag_2WO_4 phase: a joint experimental and theoretical study. *RSC Adv.* **2017**, *7* (10), 5610−5620.

(20) Lin, Z.; Li, J.; Zheng, Z.; Yan, J.; Liu, P.; Wang, C.; Yang, G. Electronic Reconstruction of α-Ag_2WO_4 Nanorods for Visible-Light Photocatalysis. *ACS Nano* **2015**, *9* (7), 7256−7265.

(21) van den Berg, A. J.; Juffermans, C. A. H. The polymorphism of silver tungstate Ag_2WO_4. *J. Appl. Crystallogr.* **1982**, *15* (1), 114−116.

(22) Longo, E.; Cavalcante, L. S.; Volanti, D. P.; Gouveia, A. F.; Longo, V. M.; Varela, J. A.; Orlandi, M. O.; Andres, J. Direct in situ observation of the electron-driven synthesis of Ag filaments on α-Ag_2WO_4 crystals. *Sci. Rep.* **2013**, *3*, 1676.

(23) Longo, E.; Avansi, W., Jr.; Bettini, J.; Andres, J.; Gracia, L. In situ Transmission Electron Microscopy observation of Ag nanocrystal evolution by surfactant free electron-driven synthesis. *Sci. Rep.* **2016**, *6*, 21498.

(24) Andres, J.; Gracia, L.; Gonzalez-Navarrete, P.; Longo, V. M.; Avansi, W., Jr.; Volanti, D. P.; Ferrer, M. M.; Lemos, P. S.; La Porta, F. A.; Hernandes, A. C.; Longo, E. Structural and electronic analysis of the atomic scale nucleation of Ag on α-Ag_2WO_4 induced by electron irradiation. *Sci. Rep.* **2015**, *4*, 5391.

(25) Cavalcante, L. S.; Almeida, M. A.; Avansi, W., Jr.; Tranquilin, R. L.; Longo, E.; Batista, N. C.; Mastelaro, V. R.; Li, M. S. Cluster coordination and photoluminescence properties of α-Ag_2WO_4 microcrystals. *Inorg. Chem.* **2012**, *51* (20), 10675−87.

(26) Roca, R. A.; Lemos, P. S.; Andrés, J.; Longo, E. Formation of Ag nanoparticles on metastable β-Ag_2WO_4 microcrystals induced by electron irradiation. *Chem. Phys. Lett.* **2016**, *644*, 68−72.

(27) Heiligtag, F. J.; Niederberger, M. The fascinating world of nanoparticle research. *Mater. Today* **2013**, *16* (7−8), 262−271.

(28) Gatoo, M. A.; Naseem, S.; Arfat, M. Y.; Dar, A. M.; Qasim, K.; Zubair, S. Physicochemical properties of nanomaterials: implication in associated toxic manifestations. *BioMed Res. Int.* **2014**, *2014*, 498420.

(29) Albanese, A.; Tang, P. S.; Chan, W. C. The effect of nanoparticle size, shape, and surface chemistry on biological systems. *Annu. Rev. Biomed. Eng.* **2012**, *14*, 1−16.

(30) Tsuzuki, T. *Nanotechnology Commercialization*; Pan Stanford Publishing: 2016.

(31) San-Miguel, M. A.; da Silva, E. Z.; Zanetti, S. M.; Cilense, M.; Fabbro, M. T.; Gracia, L.; Andres, J.; Longo, E. In situ growth of Ag nanoparticles on α-Ag_2WO_4 under electron irradiation: probing the physical principles. *Nanotechnology* **2016**, *27* (22), 225703.

(32) Botelho, G.; Sczancoski, J. C.; Andres, J.; Gracia, L.; Longo, E. Experimental and Theoretical Study on the Structure, Optical Properties, and Growth of Metallic Silver Nanostructures in Ag_3PO_4. *J. Phys. Chem. C* **2015**, *119* (11), 6293−6306.

(33) Cunha, F. S.; Sczancoski, J. C.; Nogueira, I. C.; de Oliveira, V. G.; Lustosa, S. M. C.; Longo, E.; Cavalcante, L. S. Structural, morphological and optical investigation of β-Ag_2MoO_4 microcrystals obtained with different polar solvents. *CrystEngComm* **2015**, *17* (43), 8207−8211.

(34) Lu, Y.; Shen, Q.; Yu, Q.; Zhang, F.; Li, G.; Zhang, W. Photoinduced In Situ Growth of Ag Nanoparticles on $AgNbO_3$. *J. Phys. Chem. C* **2016**, *120* (50), 28712−28716.

(35) Yu, S. H.; Liu, B.; Mo, M. S.; Huang, J. H.; Liu, X. M.; Qian, Y. T. General Synthesis of Single-Crystal Tungstate Nanorods/Nano-wires: A Facile, Low-Temperature Solution Approach. *Adv. Funct. Mater.* **2003**, *13* (8), 639−647.

(36) Liu, D.; Huang, W.; Li, L.; Liu, L.; Sun, X.; Liu, B.; Yang, B.; Guo, C. Experimental and theoretical investigation on photocatalytic activities of 1D Ag/Ag_2WO_4 nanostructures. *Nanotechnology* **2017**, *28* (38), 385702.

(37) da Silva, L. F.; Catto, A. C.; Avansi, W., Jr.; Cavalcante, L. S.; Andres, J.; Aguir, K.; Mastelaro, V. R.; Longo, E. A novel ozone gas sensor based on one-dimensional (1D) α-Ag_2WO_4 nanostructures. *Nanoscale* **2014**, *6* (8), 4058−62.

(38) da Silva, L. F.; Catto, A. C.; Avansi, W.; Cavalcante, L. S.; Mastelaro, V. R.; Andrés, J.; Aguir, K.; Longo, E. Acetone gas sensor based on α-Ag_2WO_4 nanorods obtained via a microwave-assisted hydrothermal route. *J. Alloys Compd.* **2016**, *683*, 186−190.

(39) Zhang, R.; Cui, H.; Yang, X.; Liu, H.; Tang, H.; Li, Y. Facile hydrothermal synthesis and photocatalytic activity of rod-like nanosized silver tungstate. *Micro Nano Lett.* **2012**, *7* (12), 1285−1288.

(40) Liu, X.; Hu, J.; Li, J.; Hu, Y.; Shao, Y.; Yang, H.; Tong, G.; Qian, H. Facile synthesis of Ag_2WO_4/AgCl nanorods for excellent photocatalytic properties. *Mater. Lett.* **2013**, *91*, 129−132.

(41) Dutta, D. P.; Singh, A.; Ballal, A.; Tyagi, A. K. High Adsorption Capacity for Cationic Dye Removal and Antibacterial Properties of Sonochemically Synthesized Ag_2WO_4 Nanorods. *Eur. J. Inorg. Chem.* **2014**, *2014* (33), 5724−5732.

(42) He, H.; Xue, S.; Wu, Z.; Yu, C.; Yang, K.; Peng, G.; Zhou, W.; Li, D. Sonochemical fabrication, characterization and enhanced photocatalytic performance of Ag_2S/Ag_2WO_4 composite microrods. *Chin. J.Catal.* **2016**, *37* (11), 1841−1850.

(43) Rajamohan, S.; Kumaravel, V.; Muthuramalingam, R.; Ayyadurai, S.; Abdel-Wahab, A.; Sub Kwak, B.; Kang, M.; Sreekantan, S. Fe_3O_4−Ag_2WO_4: facile synthesis, characterization and visible light assisted photocatalytic activity. *New J. Chem.* **2017**, *41* (20), 11722−11730.

(44) Ng, C. H. B.; Fan, W. Y. Preparation of highly uniform 1-dimensional α-Ag$_2$WO$_4$ nanostructures with controllable aspect ratio and study of the growth mechanism. *CrystEngComm* **2016**, *18* (41), 8010−8019.

(45) Sreedevi, A.; Priyanka, K. P.; Babitha, K. K.; Aloysius Sabu, N.; Anu, T. S.; Varghese, T. Chemical synthesis, structural characterization and optical properties of nanophase α-Ag$_2$WO$_4$. *Indian J. Phys.* **2015**, *89* (9), 889−897.

(46) Li, J.; Yu, C.; Zheng, C.; Etogo, A.; Xie, Y.; Zhong, Y.; Hu, Y. Facile formation of Ag$_2$WO$_4$/AgX (X = Cl, Br, I) hybrid nanorods with enhanced visible-light-driven photoelectrochemical properties. *Mater. Res. Bull.* **2015**, *61*, 315−320.

(47) Cushing, B. L.; Kolesnichenko, V. L.; O'Connor, C. J. Recent Advances in the Liquid-Phase Syntheses of Inorganic Nanoparticles. *Chem. Rev.* **2004**, *104* (9), 3893−3946.

(48) Wang, X.; Fu, C.; Wang, P.; Yu, H.; Yu, J. Hierarchically porous metastable β-Ag$_2$WO$_4$ hollow nanospheres: controlled synthesis and high photocatalytic activity. *Nanotechnology* **2013**, *24* (16), 165602.

(49) Qiu, F.; Zhu, X.; Guo, Q.; Dai, Y.; Xu, J.; Zhang, T. Fabrication of a novel hierarchical flower-like hollow structure Ag$_2$WO$_4$/WO$_3$ photocatalyst and its enhanced visible-light photocatalytic activity. *Powder Technol.* **2017**, *317*, 287−292.

(50) MacGregor, W. S. The Chemical and Physical Properties of DMSO. *Ann. N. Y. Acad. Sci.* **1967**, *141* (1), 3−12.

(51) Yu, Z.-W.; Quinn, P. J. Dimethyl sulfoxide: A review of its applications in cell biology. *Biosci. Rep.* **1994**, *14* (6), 259−281.

(52) Wu, X.-F.; Natte, K. The Applications of Dimethyl Sulfoxide as Reagent in Organic Synthesis. *Adv. Synth. Catal.* **2016**, *358* (3), 336−352.

(53) Rodríguez-Gattorno, G.; Díaz, D.; Rendón, L.; Hernández-Segura, G. O. Metallic Nanoparticles from Spontaneous Reduction of Silver(I) in DMSO. Interaction between Nitric Oxide and Silver Nanoparticles. *J. Phys. Chem. B* **2002**, *106* (10), 2482−2487.

(54) Tian, J.; Chen, G.; He, Z. Overcoming matrix effects: GC method development for the determination of triethylamine and dimethyl sulfoxide in a drug substance. *J. Chromatogr. Sci.* **2014**, *52* (1), 36−41.

(55) Zhai, T.; Xie, S.; Zhao, Y.; Sun, X.; Lu, X.; Yu, M.; Xu, M.; Xiao, F.; Tong, Y. Controllable synthesis of hierarchical ZnO nanodisks for highly photocatalytic activity. *CrystEngComm* **2012**, *14* (5), 1850.

(56) Wang, C.; Sun, L.; Yun, H.; Li, J.; Lai, Y.; Lin, C. Sonoelectrochemical synthesis of highly photoelectrochemically active TiO$_2$ nanotubes by incorporating CdS nanoparticles. *Nanotechnology* **2009**, *20* (29), 295601.

(57) Song, R.; Feng, S.; Wang, H.; Hou, C. Effect of organic solvents on particle size of Mn$_3$O$_4$ nanoparticles synthesized by a solvothermal method. *J. Solid State Chem.* **2013**, *202*, 57−60.

(58) Lu, X.-H.; Wang, D.; Li, G.-R.; Su, C.-Y.; Kuang, D.-B.; Tong, Y.-X. Controllable Electrochemical Synthesis of Hierarchical ZnO Nanostructures on FTO Glass. *J. Phys. Chem. C* **2009**, *113* (31), 13574−13582.

(59) Guin, D.; Manorama, S. V.; Radha, S.; Nigam, A. One-pot size and shape controlled synthesis of DMSO capped iron oxide nanoparticles. *Bull. Mater. Sci.* **2006**, *29* (6), 617−621.

(60) Phaomei, G.; Rameshwor Singh, W.; Ningthoujam, R. S. Solvent effect in monoclinic to hexagonal phase transformation in LaPO$_4$:RE (RE = Dy^{3+}, Sm^{3+}) nanoparticles: Photoluminescence study. *J. Lumin.* **2011**, *131* (6), 1164−1171.

(61) Fairley, N. *CasaXPS: Spectrum Processing Software for XPS, AES and SIMS*, Version 2.3.15; Casa Software Ltd.: Cheshire, U.K., 2009 (http://www.casaxps.com/).

(62) Pereira, P. F. S.; Santos, C. C.; Gouveia, A. F.; Ferrer, M. M.; Pinatti, I. M.; Botelho, G.; Sambrano, J. R.; Rosa, I. L. V.; Andres, J.; Longo, E. α-Ag$_{2−2x}$Zn$_x$WO$_4$ (0 < x < 0.25) Solid Solutions: Structure, Morphology, and Optical Properties. *Inorg. Chem.* **2017**, *56* (13), 7360−7372.

(63) Pereira, W. S.; Ferrer, M. M.; Botelho, G.; Gracia, L.; Nogueira, I. C.; Pinatti, I. M.; Rosa, I. L. V.; La Porta, F. d. A.; Andres, J.; Longo, E., Effects of chemical substitution on the structural and optical properties of α-Ag$_{2−2x}$Ni$_x$WO$_4$ (0 < x < 0.08) solid solutions. *Phys. Chem. Chem. Phys.* **2016**, *18* (31), 21966−21975.

(64) Momma, K.; Izumi, F. VESTA 3 for three-dimensional visualization of crystal, volumetric and morphology data. *J. Appl. Crystallogr.* **2011**, *44* (6), 1272−1276.

(65) Cavinato, A. G.; Mamantov, G.; Cox, X. B. Characterization of Low Oxidation States of Tungsten and Tungsten Electrodes in AlCl$_3$ - NaCl Melts by X-Ray Photoelectron Spectroscopy. *J. Electrochem. Soc.* **1985**, *132* (5), 1136−1140.

(66) Xie, F. Y.; Gong, L.; Liu, X.; Tao, Y. T.; Zhang, W. H.; Chen, S. H.; Meng, H.; Chen, J. XPS studies on surface reduction of tungsten oxide nanowire film by Ar$^+$ bombardment. *J. Electron Spectrosc. Relat. Phenom.* **2012**, *185* (3−4), 112−118.

(67) Song, J. G.; Ryu, G. H.; Lee, S. J.; Sim, S.; Lee, C. W.; Choi, T.; Jung, H.; Kim, Y.; Lee, Z.; Myoung, J. M.; Dussarrat, C.; Lansalot-Matras, C.; Park, J.; Choi, H.; Kim, H. Controllable synthesis of molybdenum tungsten disulfide alloy for vertically composition-controlled multilayer. *Nat. Commun.* **2015**, *6*, 7817.

(68) Bai, H.; Su, N.; Li, W.; Zhang, X.; Yan, Y.; Li, P.; Ouyang, S.; Ye, J.; Xi, G. W$_{18}$O$_{49}$ nanowire networks for catalyzed dehydration of isopropyl alcohol to propylene under visible light. *J. Mater. Chem. A* **2013**, *1* (20), 6125.

(69) Kondalkar, V. V.; Mali, S. S.; Kharade, R. R.; Mane, R. M.; Patil, P. S.; Hong, C. K.; Kim, J. H.; Choudhury, S.; Bhosale, P. N. Langmuir−Blodgett self organized nanocrystalline tungsten oxide thin films for electrochromic performance. *RSC Adv.* **2015**, *5* (34), 26923−26931.

(70) Li, H.; Zhou, Y.; Chen, L.; Luo, W.; Xu, Q.; Wang, X.; Xiao, M.; Zou, Z. Rational and scalable fabrication of high-quality WO$_3$/CdS core/shell nanowire arrays for photoanodes toward enhanced charge separation and transport under visible light. *Nanoscale* **2013**, *5* (23), 11933−9.

(71) Zhang, H.; Wang, G.; Chen, D.; Lv, X.; Li, J. Tuning Photoelectrochemical Performances of Ag−TiO$_2$ Nanocomposites via Reduction/Oxidation of Ag. *Chem. Mater.* **2008**, *20* (20), 6543−6549.

(72) Cai, L.; Xiong, X.; Liang, N.; Long, Q. Highly effective and stable Ag$_3$PO$_4$−WO$_3$/MWCNTs photocatalysts for simultaneous Cr(VI) reduction and orange II degradation under visible light irradiation. *Appl. Surf. Sci.* **2015**, *353*, 939−948.

(73) Celebioglu, A.; Vempati, S.; Ozgit-Akgun, C.; Biyikli, N.; Uyar, T. Water-soluble non-polymeric electrospun cyclodextrin nanofiber template for the synthesis of metal oxide tubes by atomic layer deposition. *RSC Adv.* **2014**, *4* (106), 61698−61705.

(74) Zhao, C. X.; Deng, S. Z.; Xu, N. S.; Chen, J. Correlation between surface chemistry, gasochromism and field emission properties of tungsten oxide nanowire thin films when exposed to atomic oxygen. *RSC Adv.* **2015**, *5* (86), 70059−70063.

(75) Chen, Z.; Bing, F.; Liu, Q.; Zhang, Z.; Fang, X. Novel Z-scheme visible-light-driven Ag$_3$PO$_4$/Ag/SiC photocatalysts with enhanced photocatalytic activity. *J. Mater. Chem. A* **2015**, *3* (8), 4652−4658.

(76) Andres, J.; Gracia, L.; Gouveia, A. F.; Ferrer, M. M.; Longo, E. Effects of surface stability on the morphological transformation of metals and metal oxides as investigated by first-principles calculations. *Nanotechnology* **2015**, *26* (40), 405703.

(77) Gong, J.; Liu, H.; Jiang, Y.; Yang, S.; Liao, X.; Liu, Z.; Ringer, S. In-situ synthesis of Ag nanoparticles by electron beam irradiation. *Mater. Charact.* **2015**, *110*, 1−4.

(78) http://www2.fiz-karlsruhe.de/icsd_price_list.html (last acess - 26/11/17).

(79) Wagner, C. Theorie der Alterung von Niederschlägen durch Umlösen (Ostwald-Reifung). *Zeitschrift für Elektrochemie, Berichte der Bunsengesellschaft für physikalische Chemie* **1961**, *65* (7−8), 581−591.

(80) Penn, R. L. Imperfect Oriented Attachment: Dislocation Generation in Defect-Free Nanocrystals. *Science* **1998**, *281* (5379), 969−971.

(81) Penn, R. L.; Banfield, J. F. Oriented attachment and growth, twinning, polytypism, and formation of metastable phases; insights

from nanocrystalline TiO$_2$. *Am. Mineral.* **1998**, *83* (9−10), 1077−1082.

(82) Egerton, R. F.; Li, P.; Malac, M. Radiation damage in the TEM and SEM. *Micron* **2004**, *35* (6), 399−409.

(83) Gonzalez-Martinez, I. G.; Bachmatiuk, A.; Bezugly, V.; Kunstmann, J.; Gemming, T.; Liu, Z.; Cuniberti, G.; Rummeli, M. H. Electron-beam induced synthesis of nanostructures: a review. *Nanoscale* **2016**, *8* (22), 11340−62.

(84) Rahaman, M. N. *Ceramic Processing*, 2nd ed.; CRC Press: 2017.

(85) Jain, V. K. *Nanofinishing Science and Technology: Basic and Advanced Finishing and Polishing Processes*; CRC Press: 2016.